Measurement of transverse single-spin asymmetries of π^0 and electromagnetic jets at forward rapidity in 200 and 500 GeV transversely polarized proton-proton collisions

J. Adam,[6] L. Adamczyk,[2] J. R. Adams,[33] J. K. Adkins,[55] G. Agakishiev,[22] M. M. Aggarwal,[34] Z. Ahammed,[62] I. Alekseev,[3,28] D. M. Anderson,[45] A. Aparin,[22] E. C. Aschenauer,[6] M. U. Ashraf,[7] F. G. Atetalla,[23] A. Attri,[34] G. S. Averichev,[22] V. Bairathi,[21] K. Barish,[50] A. Behera,[42] R. Bellwied,[53] A. Bhasin,[54] J. Bielcik,[9] J. Bielcikova,[31] L. C. Bland,[6] I. G. Bordyuzhin,[3] J. D. Brandenburg,[6] A. V. Brandin,[28] J. Butterworth,[37] H. Caines,[65] M. Calderón de la Barca Sánchez,[48] D. Cebra,[48] I. Chakaberia,[23,6] P. Chaloupka,[9] B. K. Chan,[49] F-H. Chang,[30] Z. Chang,[6] N. Chankova-Bunzarova,[22] A. Chatterjee,[7] D. Chen,[50] J. Chen,[39] J. H. Chen,[12] X. Chen,[57] Z. Chen,[39] J. Cheng,[46] M. Cherney,[8] M. Chevalier,[50] S. Choudhury,[12] W. Christie,[6] X. Chu,[6] H. J. Crawford,[47] M. Csanád,[10] M. Daugherity,[1] T. G. Dedovich,[22] I. M. Deppner,[52] A. A. Derevschikov,[32] L. Didenko,[6] C. Dilks,[35] X. Dong,[24] J. L. Drachenberg,[1] J. C. Dunlop,[6] T. Edmonds,[36] N. Elsey,[64] J. Engelage,[47] G. Eppley,[37] S. Esumi,[59] O. Evdokimov,[51] A. Ewigleben,[25] O. Eyser,[6] R. Fatemi,[55] S. Fazio,[6] P. Federic,[31] J. Fedorisin,[22] C. J. Feng,[30] Y. Feng,[36] P. Filip,[22] E. Finch,[41] Y. Fisyak,[6] A. Francisco,[65] L. Fulek,[2] C. A. Gagliardi,[45] T. Galatyuk,[43] F. Geurts,[37] N. Ghimire,[44] A. Gibson,[61] K. Gopal,[15] X. Gou,[39] D. Grosnick,[61] W. Guryn,[6] A. I. Hamad,[23] A. Hamed,[5] S. Harabasz,[43] J. W. Harris,[65] S. He,[7] W. He,[12] X. H. He,[18] Y. He,[39] S. Heppelmann,[48] S. Heppelmann,[35] N. Herrmann,[52] E. Hoffman,[53] L. Holub,[9] Y. Hong,[24] S. Horvat,[65] Y. Hu,[12] H. Z. Huang,[49] S. L. Huang,[42] T. Huang,[30] X. Huang,[46] T. J. Humanic,[33] P. Huo,[42] G. Igo,[49†] D. Isenhower,[1] W. W. Jacobs,[17] C. Jena,[15] A. Jentsch,[6] Y. Ji,[57] J. Jia,[6,42] K. Jiang,[57] S. Jowzaee,[64] X. Ju,[57] E. G. Judd,[47] S. Kabana,[21] M. L. Kabir,[50] S. Kagamaster,[25] D. Kalinkin,[17] K. Kang,[46] D. Kapukchyan,[50] K. Kauder,[6] H. W. Ke,[6] D. Keane,[23] A. Kechechyan,[22] M. Kelsey,[24] Y. V. Khyzhniak,[28] D. P. Kikoła,[63] C. Kim,[50] B. Kimelman,[48] D. Kincses,[10] T. A. Kinghorn,[48] I. Kisel,[11] A. Kiselev,[6] M. Kocan,[9] L. Kochenda,[28] L. K. Kosarzewski,[9] L. Kramarik,[9] P. Kravtsov,[28] K. Krueger,[4] N. Kulathunga Mudiyanselage,[53] L. Kumar,[34] S. Kumar,[18] R. Kunnawalkam Elayavalli,[64] J. H. Kwasizur,[17] R. Lacey,[42] S. Lan,[7] J. M. Landgraf,[6] J. Lauret,[6] A. Lebedev,[6] R. Lednicky,[22] J. H. Lee,[6] Y. H. Leung,[24] C. Li,[39] C. Li,[57] W. Li,[37] W. Li,[40] X. Li,[57] Y. Li,[46] Y. Liang,[23] R. Licenik,[31] T. Lin,[45] Y. Lin,[7] M. A. Lisa,[33] F. Liu,[7] H. Liu,[17] P. Liu,[42] P. Liu,[40] T. Liu,[65] X. Liu,[33] Y. Liu,[45] Z. Liu,[57] T. Ljubicic,[6] W. J. Llope,[64] R. S. Longacre,[6] N. S. Lukow,[44] S. Luo,[51] X. Luo,[7] G. L. Ma,[40] L. Ma,[12] R. Ma,[6] Y. G. Ma,[40] N. Magdy,[51] R. Majka,[65†] D. Mallick,[29] S. Margetis,[23] C. Markert,[58] H. S. Matis,[24] J. A. Mazer,[38] N. G. Minaev,[32] S. Mioduszewski,[45] B. Mohanty,[29] M. M. Mondal,[19] I. Mooney,[64] Z. Moravcova,[9] D. A. Morozov,[32] M. Nagy,[10] J. D. Nam,[44] Md. Nasim,[14] K. Nayak,[7] D. Neff,[49] J. M. Nelson,[47] D. B. Nemes,[65] M. Nie,[39] G. Nigmatkulov,[28] T. Niida,[59] L. V. Nogach,[32] T. Nonaka,[59] A. S. Nunes,[6] G. Odyniec,[24] A. Ogawa,[6] S. Oh,[24] V. A. Okorokov,[28] B. S. Page,[6] R. Pak,[6] A. Pandav,[29] Y. Panebratsev,[22] B. Pawlik,[20] D. Pawlowska,[63] H. Pei,[7] C. Perkins,[47] L. Pinsky,[53] R. L. Pintér,[10] J. Pluta,[63] B. R. Pokhrel,[44] J. Porter,[24] M. Posik,[44] N. K. Pruthi,[34] M. Przybycien,[2] J. Putschke,[64] H. Qiu,[18] A. Quintero,[44] S. K. Radhakrishnan,[23] S. Ramachandran,[55] R. L. Ray,[58] R. Reed,[25] H. G. Ritter,[24] O. V. Rogachevskiy,[22] J. L. Romero,[48] L. Ruan,[6] J. Rusnak,[31] N. R. Sahoo,[39] H. Sako,[59] S. Salur,[38] J. Sandweiss,[65†] S. Sato,[59] W. B. Schmidke,[6] N. Schmitz,[26] B. R. Schweid,[42] F. Seck,[43] J. Seger,[8] M. Sergeeva,[49] R. Seto,[50] P. Seyboth,[26] N. Shah,[16] E. Shahaliev,[22] P. V. Shanmuganathan,[6] M. Shao,[57] A. I. Sheikh,[23] W. Q. Shen,[40] S. S. Shi,[7] Y. Shi,[39] Q. Y. Shou,[40] E. P. Sichtermann,[24] R. Sikora,[2] M. Simko,[31] J. Singh,[34] S. Singha,[18] N. Smirnov,[65] W. Solyst,[17] P. Sorensen,[6] H. M. Spinka,[4†] B. Srivastava,[36] T. D. S. Stanislaus,[61] M. Stefaniak,[63] D. J. Stewart,[65] M. Strikhanov,[28] B. Stringfellow,[36] A. A. P. Suaide,[56] M. Sumbera,[31] B. Summa,[35] X. M. Sun,[7] X. Sun,[51] Y. Sun,[57] Y. Sun,[13] B. Surrow,[44] D. N. Svirida,[3] P. Szymanski,[63] A. H. Tang,[6] Z. Tang,[57] A. Taranenko,[28] T. Tarnowsky,[27] J. H. Thomas,[24] A. R. Timmins,[53] D. Tlusty,[8] M. Tokarev,[22] C. A. Tomkiel,[25] S. Trentalange,[49] R. E. Tribble,[45] P. Tribedy,[6] S. K. Tripathy,[10] O. D. Tsai,[49] Z. Tu,[6] T. Ullrich,[6] D. G. Underwood,[4] I. Upsal,[39,6] G. Van Buren,[6] J. Vanek,[31] A. N. Vasiliev,[32] I. Vassiliev,[11] F. Videbæk,[6] S. Vokal,[22] S. A. Voloshin,[64] F. Wang,[36] G. Wang,[49] J. S. Wang,[13] P. Wang,[57] Y. Wang,[7] Y. Wang,[46] Z. Wang,[39] J. C. Webb,[6] P. C. Weidenkaff,[52] L. Wen,[49] G. D. Westfall,[27] H. Wieman,[24] S. W. Wissink,[17] R. Witt,[60] Y. Wu,[50] Z. G. Xiao,[46] G. Xie,[24] W. Xie,[36] H. Xu,[13] N. Xu,[24] Q. H. Xu,[39] Y. F. Xu,[40] Y. Xu,[39] Z. Xu,[6] Z. Xu,[49] C. Yang,[39] Q. Yang,[39] S. Yang,[6] Y. Yang,[30] Z. Yang,[7] Z. Ye,[37] Z. Ye,[51] L. Yi,[39] K. Yip,[6] Y. Yu,[39] H. Zbroszczyk,[63] W. Zha,[57] C. Zhang,[42] D. Zhang,[7] S. Zhang,[57] S. Zhang,[40] X. P. Zhang,[46] Y. Zhang,[57] Y. Zhang,[7] Z. J. Zhang,[30] Z. Zhang,[6] Z. Zhang,[51] J. Zhao,[36] C. Zhong,[40] C. Zhou,[40] X. Zhu,[46] Z. Zhu,[39] M. Zurek,[24] and M. Zyzak[11]

(STAR Collaboration)

[1]*Abilene Christian University, Abilene, Texas 79699*
[2]*AGH University of Science and Technology, FPACS, Cracow 30-059, Poland*

[3]*Alikhanov Institute for Theoretical and Experimental Physics NRC "Kurchatov Institute", Moscow 117218, Russia*
[4]*Argonne National Laboratory, Argonne, Illinois 60439*
[5]*American University of Cairo, New Cairo 11835, New Cairo, Egypt*
[6]*Brookhaven National Laboratory, Upton, New York 11973*
[7]*Central China Normal University, Wuhan, Hubei 430079*
[8]*Creighton University, Omaha, Nebraska 68178*
[9]*Czech Technical University in Prague, FNSPE, Prague 115 19, Czech Republic*
[10]*ELTE Eötvös Loránd University, Budapest H-1117, Hungary*
[11]*Frankfurt Institute for Advanced Studies FIAS, Frankfurt 60438, Germany*
[12]*Fudan University, Shanghai 200433*
[13]*Huzhou University, Huzhou, Zhejiang 313000*
[14]*Indian Institute of Science Education and Research (IISER), Berhampur 760010, India*
[15]*Indian Institute of Science Education and Research (IISER) Tirupati, Tirupati 517507, India*
[16]*Indian Institute Technology, Patna, Bihar 801106, India*
[17]*Indiana University, Bloomington, Indiana 47408*
[18]*Institute of Modern Physics, Chinese Academy of Sciences, Lanzhou, Gansu 730000*
[19]*Institute of Physics, Bhubaneswar 751005, India*
[20]*Institute of Nuclear Physics PAN, Cracow 31-342, Poland*
[21]*Instituto de Alta Investigación, Universidad de Tarapacá, Arica 1000000, Chile*
[22]*Joint Institute for Nuclear Research, Dubna 141 980, Russia*
[23]*Kent State University, Kent, Ohio 44242*
[24]*Lawrence Berkeley National Laboratory, Berkeley, California 94720*
[25]*Lehigh University, Bethlehem, Pennsylvania 18015*
[26]*Max-Planck-Institut für Physik, Munich 80805, Germany*
[27]*Michigan State University, East Lansing, Michigan 48824*
[28]*National Research Nuclear University MEPhI, Moscow 115409, Russia*
[29]*National Institute of Science Education and Research, HBNI, Jatni 752050, India*
[30]*National Cheng Kung University, Tainan 70101*
[31]*Nuclear Physics Institute of the CAS, Rez 250 68, Czech Republic*
[32]*NRC "Kurchatov Institute", Institute of High Energy Physics, Protvino 142281, Russia*
[33]*Ohio State University, Columbus, Ohio 43210*
[34]*Panjab University, Chandigarh 160014, India*
[35]*Pennsylvania State University, University Park, Pennsylvania 16802*
[36]*Purdue University, West Lafayette, Indiana 47907*
[37]*Rice University, Houston, Texas 77251*
[38]*Rutgers University, Piscataway, New Jersey 08854*
[39]*Shandong University, Qingdao, Shandong 266237*
[40]*Shanghai Institute of Applied Physics, Chinese Academy of Sciences, Shanghai 201800*
[41]*Southern Connecticut State University, New Haven, Connecticut 06515*
[42]*State University of New York, Stony Brook, New York 11794*
[43]*Technische Universität Darmstadt, Darmstadt 64289, Germany*
[44]*Temple University, Philadelphia, Pennsylvania 19122*
[45]*Texas A&M University, College Station, Texas 77843*
[46]*Tsinghua University, Beijing 100084*
[47]*University of California, Berkeley, California 94720*
[48]*University of California, Davis, California 95616*
[49]*University of California, Los Angeles, California 90095*
[50]*University of California, Riverside, California 92521*
[51]*University of Illinois at Chicago, Chicago, Illinois 60607*
[52]*University of Heidelberg, Heidelberg 69120, Germany*
[53]*University of Houston, Houston, Texas 77204*
[54]*University of Jammu, Jammu 180001, India*
[55]*University of Kentucky, Lexington, Kentucky 40506-0055*
[56]*Universidade de São Paulo, São Paulo 05314-970, Brazil*
[57]*University of Science and Technology of China, Hefei, Anhui 230026*
[58]*University of Texas, Austin, Texas 78712*
[59]*University of Tsukuba, Tsukuba, Ibaraki 305-8571, Japan*
[60]*United States Naval Academy, Annapolis, Maryland 21402*
[61]*Valparaiso University, Valparaiso, Indiana 46383*

[62]Variable Energy Cyclotron Centre, Kolkata 700064, India
[63]Warsaw University of Technology, Warsaw 00-661, Poland
[64]Wayne State University, Detroit, Michigan 48201
[65]Yale University, New Haven, Connecticut 06520

(Received 21 December 2020; accepted 29 March 2021; published 27 May 2021)

The STAR Collaboration reports measurements of the transverse single-spin asymmetry (TSSA) of inclusive π^0 at center-of-mass energies ($\sqrt{s}$) of 200 GeV and 500 GeV in transversely polarized proton-proton collisions in the pseudo-rapidity region 2.7 to 4.0. The results at the two different energies show a continuous increase of the TSSA with Feynman-x, and, when compared to previous measurements, no dependence on $\sqrt{s}$ from 19.4 GeV to 500 GeV is found. To investigate the underlying physics leading to this large TSSA, different topologies have been studied. π^0 with no nearby particles tend to have a higher TSSA than inclusive π^0. The TSSA for inclusive electromagnetic jets, sensitive to the Sivers effect in the initial state, is substantially smaller, but shows the same behavior as the inclusive π^0 asymmetry as a function of Feynman-x. To investigate final-state effects, the Collins asymmetry of π^0 inside electromagnetic jets has been measured. The Collins asymmetry is analyzed for its dependence on the π^0 momentum transverse to the jet thrust axis and its dependence on the fraction of jet energy carried by the π^0. The asymmetry was found to be small in each case for both center-of-mass energies. All the measurements are compared to QCD-based theoretical calculations for transverse-momentum-dependent parton distribution functions and fragmentation functions. Some discrepancies are found, which indicates new mechanisms might be involved.

DOI: 10.1103/PhysRevD.103.092009

I. INTRODUCTION

Significant transverse single-spin asymmetries (TSSA) have been observed for charged- and neutral-hadron production in hadron-hadron collisions over a wide range of collision energies since the 1970s [1–5]. The early leading-order QCD calculation showed the corresponding asymmetry is exceedingly small [6]. Different models and mechanisms have been proposed to understand these sizable asymmetries [7–9]. Recently, all of the QCD-based formalisms for TSSA have been categorized into two frameworks. The first one is based on transverse-momentum-dependent (TMD) parton distribution or fragmentation functions, and the second one is based on Twist-3 collinear factorization. These two ansätze probe different underlying subprocesses. In the TMD framework one requires two scales, a large momentum transfer Q as a "hard" scale, and a modest transverse momentum q_{T} as a "soft" scale. In general one requires $Q \gg q_{\mathrm{T}}$. Calculations in the Twist-3 framework only require one scale with $q_{\mathrm{T}} \gg \Lambda_{\mathrm{QCD}}$, the strong interaction scale. It has been proven [10] that both approaches describe the same physics in the kinematic region where they overlap, i.e., $Q \gg q_{\mathrm{T}} \gg \Lambda_{\mathrm{QCD}}$.

For both frameworks, the origin of the hadron TSSA in hadron-hadron collisions can have two sources, namely an initial-state and a final-state effect. In the pure TMD approach, the initial-state effect is from the Sivers function ($f_{1\mathrm{T}}^{\perp,q}$) [11], and the final-state effect is from the coupling of the chiral-odd transversity parton distribution function and the chiral-odd Collins fragmentation function ($H_1^{\perp}$) [12,13]. The counterpart of the Sivers function in Twist-3 collinear factorization is the Efremov-Teryaev-Qui-Sterman (ETQS) function ($T_{q,F}$) [14,15]. It has been shown that $T_{q,F}$ is related to the Sivers function [16] through the following relation:

$$T_{q,F}(x,x) = -\int d^2k_\perp \frac{|k_\perp^2|}{M} f_{1T}^{\perp,q}(x,k_\perp^2)|_{\mathrm{SIDIS}}. \quad (1)$$

Therefore the Sivers function extracted from semi-inclusive deep-inelastic scattering (SIDIS) data can be used to constrain the ETQS-function in transversely polarized proton-proton collisions. A very similar relation holds for the Collins fragmentation function equivalent in the Twist-3 formalism [17].

In the measurements discussed in this paper, the large transverse momentum (p_{T}) of the final-state π^0 fits the scale requirement of the Twist-3 formalism. Many phenomenological studies of the pion TSSA have been done in the Twist-3 framework. The contributions from initial-state effects [18–21], final-state effects [17,22–24], and their combination [25,26] have been calculated. For

[†]Deceased.

many years the initial-state effect was thought to be the main source of the TSSA. However, it has been realized that the ETQS-function extracted from proton-proton collisions and the Sivers function extracted from SIDIS do not coincide well [25]. In recent years, it was proposed that the initial-state effects are small and the final-state effects are the main contribution to the TSSA [26,27].

The initial-state and final-state effects cannot be disentangled for the pion TSSA, but other observables such as the jet TSSA and Collins asymmetry can be used to separate them. The TSSA for jets is considered to be sensitive to initial-state effects. An earlier measurement in transversely polarized proton-proton collisions at $\sqrt{s} = 500$ GeV by the $A_N DY$ experiment found the inclusive jet TSSA to be very small [28]. This was reproduced by theoretical calculations [29,30] of the jet TSSA. On the other hand, the Collins asymmetry is only sensitive to final-state effects. It measures the azimuthal asymmetry of a hadron within a jet originating from the fragmentation of a transversely polarized quark. Theory predictions for the Collins asymmetry in transversely polarized proton-proton collisions can be found in Refs. [31–33]. Experimental results at mid-rapidity have been reported by the STAR (Solenoidal Tracker At Relativistic Heavy Ion Collider) Collaboration [34].

In this paper, the STAR Collaboration at the RHIC reports new measurements of the TSSA for the inclusive π^0 production at large rapidity in transversely polarized proton-proton collisions at $\sqrt{s}$ of 200 and 500 GeV to study the energy dependence of the TSSA. To understand the underlying physics mechanisms, different topologies for the TSSA have been investigated, which include the extraction of the TSSA for inclusive and isolated π^0, electromagnetic jets, and the Collins effect through π^0 inside an electromagnetic jet. Recently STAR published a complementary study of the nuclear dependence of the π^0 TSSA [35], which used the same 200 GeV proton-proton data that are investigated here. Although some technical aspects of the two analyses slightly differ, the results are consistent in those cases where the same quantity is measured.

This paper is organized as follows. Section II provides the analysis details including a brief overview of RHIC and the Forward Meson Spectrometer (FMS) detector, event selection, π^0 and jet reconstruction, and the methods of spin asymmetry calculation. The correction and systematic uncertainty studies are discussed in Sec. III. Section IV gives the TSSA results for inclusive π^0, isolated π^0 and jets, and the Collins asymmetry results for π^0. Finally, Sec. V presents a summary of the measurements.

II. ANALYSIS

A. Experiment

The measurements have been performed with the STAR detector [36] at RHIC located at Brookhaven National Laboratory. RHIC is currently the only facility in the world that can provide high energy, high luminosity, highly polarized proton-proton collisions. The clockwise and counterclockwise proton beams at RHIC are labeled as blue and yellow, respectively. The beam polarization measurements are provided by the RHIC polarimeter group, which develops, maintains, and operates the RHIC polarimeters. The details of the beam polarization measurements in recent years can be found in Ref. [37].

The analysis in this paper uses the FMS detector at STAR to reconstruct photons and π^0s. The FMS is an electromagnetic calorimeter installed on the west side of the STAR detector, about seven meters away from the interaction point. It faces the blue beam with a pseudo-rapidity coverage of about $2.6 < \eta < 4.1$. The layout of the FMS is shown in Fig. 1. The FMS has an octagonal shape with a radius of about 1 m surrounding the beam pipe with a 40 cm × 40 cm central cutout. The FMS is made of 1264 lead glass towers of two types, which differ in size and density of towers. The towers closer to the beam line are smaller in size in order to separate photons from high energy π^0 decays. The inner towers are 3.8 cm × 3.8 cm × 45 cm in size and cover a pseudo-rapidity range from 3.3 to 4.1. The outer towers are larger, 5.8 cm × 5.8 cm × 60 cm in size, and cover a pseudo-rapidity range from 2.6 to 3.3. All towers are wrapped in thin aluminized mylar for optical isolation. Both tower types have more than 18 radiation lengths, so photons deposit nearly all of their energy in the detector. A detailed description of the detector can be found in Refs. [38–40].

The calibration of the FMS is based on the invariant mass of the reconstructed π^0. Since the decay photons from the π^0 cover multiple towers, iterations are performed until the gains of all the towers have converged.

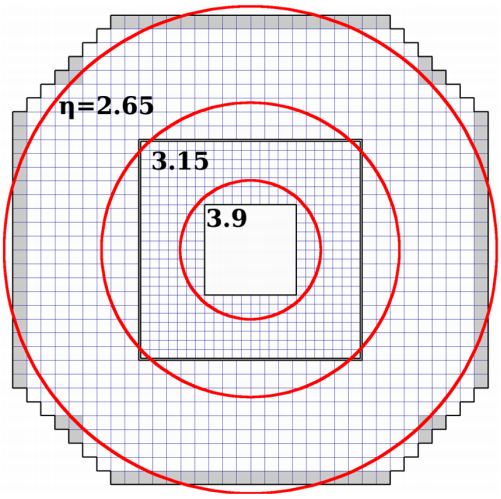

FIG. 1. The layout of the FMS detector [39].

B. Event selection

The data sets used in this paper were collected by STAR in 2011 and 2015 from transversely polarized proton-proton collisions at $\sqrt{s}$ of 500 and 200 GeV, respectively. The beam polarization of the data set is $52.4 \pm 1.8\%$ for the blue beam, which faces the FMS, in 2011 and $56.6 \pm 1.7\%$ for the blue beam in 2015.

The proton-proton collision events were triggered by the FMS itself, based on the total transverse energy (E_{T}) deposited in the detector. There were two types of triggers used in the analysis, which differ in how the regions for the energy deposition were chosen. The Board Sum triggers were based on the energy sum of overlapping areas, which covered a patch of 4×8 adjacent towers. The Jet Patch triggers used combinations of several nonoverlapping Board Sum regions. Each Jet Patch covered a quarter of the FMS with a $\pi/2$ coverage in azimuth. In 2011, there were four patches, with each covering one quadrant. In 2015, two additional patches straddling the horizontal axis were added to smooth the acceptance. In order to avoid a possible bias from the Board Sum triggers, only Jet Patch triggered data were used in the jet TSSA analysis.

Each trigger condition was operated with multiple E_{T} thresholds. The thresholds for the small-tower Board Sum triggers were 1.6/2.7 GeV in 2011 and 1.3/1.8/2.2/2.5 GeV in 2015. For the large-tower Board Sum triggers, the thresholds were 2.7/4.3 GeV in 2011 and 1.3/1.8/2.8 GeV in 2015. For the Jet Patch triggers, the thresholds are 2.7/4.3 GeV in 2011 and 1.8/2.8/3.7 GeV in 2015. The triggers with the lower thresholds were prescaled due to the limited bandwidth of the STAR data acquisition system. In the π^0/EM-jet TSSA analysis, the π^0/EM-jet p_{T} is required to be larger than the trigger threshold of the event.

The longitudinal vertex position (z-vertex) of FMS events was provided by the Beam Beam Counters (BBC) at STAR [41]. The z-vertex selection for 500 GeV data was $-68\ \mathrm{cm} < z < 68\ \mathrm{cm}$, and $-126\ \mathrm{cm} < z < 54\ \mathrm{cm}$ for 200 GeV data. The latter vertex range was biased towards the negative direction due to the FMS trigger system setup in 2015.

In 2015, the installation of the Heavy Flavor Tracker [42] in STAR introduced some noncollision background, which has an impact on the jet TSSA analysis. In the jet selection, these events are removed effectively with cuts based on information from the BBC and Time-of-Flight (TOF) [43] subdetectors. For the east BBC, which covers the pseudo-rapidity range $-5 < \eta < -3.2$ on the opposite side of STAR from the FMS, it was required that at least one tile fired. For the TOF, which covers the mid-rapidity region $-0.9 < \eta < 0.9$, its multiplicity was required to be greater than two. The noncollision background was found to affect the π^0 analysis much less, such that the above cuts were not applied.

C. π^0 reconstruction and selection

There are three major steps in reconstructing a π^0 candidate in the FMS: cluster finding, shower shape fitting, and photon combination. The first step is to incorporate the adjacent towers with nonzero energy into clusters. A minimum energy threshold of 0.5 GeV for 200 GeV data and 1.0 GeV for 500 GeV data is applied to the reconstructed clusters to reject part of the charged hadron background. Due to the finite tower size, decay photons from a high energy π^0 tend to merge into one cluster, so the clusters need to be classified as one-photon-type or two-photon-type based on their size and energy distribution. After the clusters are found, a shower shape fitting procedure is applied to determine the energy and position of the photon candidate(s) for each cluster. An ideal shape of an electromagnetic shower is compared to the actual energy pattern of a cluster in the fitting. For a two-photon-type cluster, the separation between the two photons and their energy sharing are additional degrees of freedom that need to be determined. In the end, a list of photon candidates is generated and all pairs are used to build π^0 candidates.

Further π^0 selection includes a fiducial volume cut for the photons and other cuts for the π^0 candidates described below. The fiducial volume cut requires the photon position to be at least half of a tower width away from the outer and inner edge of the detector. For the π^0 reconstruction, there are further requirements such as the following:

(i) $p_{\mathrm{T}} > 2\ \mathrm{GeV}/c$,
(ii) $2.7 < \eta < 4.0$,
(iii) $M_{\gamma\gamma} < 0.3\ \mathrm{GeV}/c^2$,
(iv) $Z_{\gamma\gamma} = |\frac{E_1 - E_2}{E_1 + E_2}| < 0.7$, where E_1 and E_2 are the energies of two photons.

Figure 2 shows an example of the invariant mass distribution of the reconstructed π^0 in 500 GeV proton-proton collision data. The data were fit to determine the signal fraction in the signal region (0.0–0.2 GeV/c^2) and sideband region (0.2–0.3 GeV/c^2). In this paper, skewed Gaussian functions in Eq. (2) are used to fit the signal and background shapes. The skewed Gaussian function has three shape parameters: the mean (ξ), the width (ω), and the skewness (α). The expected signal and background shape parameters for the two-photon invariant mass distribution in each π^0 energy bin are extracted from Monte Carlo (MC) simulation. The parameters of the skewed Gaussian functions are allowed to vary during fitting by 10–20% depending on energy. The MC simulation used the standard STAR simulation framework based on GEANT 3 [44], and PYTHIA 6.428 [45] as event generator with the CDF tune A [46]:

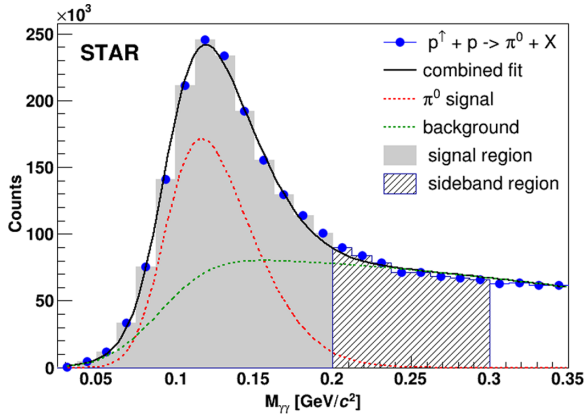

FIG. 2. Example of invariant mass spectrum of the reconstructed gamma pairs in the FMS with an energy 38 GeV $< E_{\gamma\gamma} <$ 43 GeV in transversely polarized proton-proton collisions at $\sqrt{s} = 500$ GeV. The mass spectrum is divided into signal region (0.0–0.2 GeV$/c^2$) and the sideband region (0.2–0.3 GeV$/c^2$). The dashed lines are the fit results for the π^0 signal and background. The solid line is the combined fit result.

$$f(x) = \frac{2}{\omega}\phi\left(\frac{x-\xi}{\omega}\right)\Phi\left(\alpha\cdot\frac{x-\xi}{\omega}\right),$$
$$\phi(x) = \frac{1}{\sqrt{2\pi}}e^{-\frac{x^2}{2}},$$
$$\Phi(x) = \int_{-\infty}^{x}\phi(t)dt = \frac{1}{2}\left[1+\mathrm{erf}\left(\frac{x}{\sqrt{2}}\right)\right]. \quad (2)$$

For the π^0 in a jet, which is used in studying the Collins asymmetry, the π^0 reconstruction is slightly different and will be discussed in Sec. II E 2 in detail.

D. Jet reconstruction

In the measurement of the jet TSSA and the Collins asymmetry, the jet reconstruction is needed. In this paper, the jet reconstruction is based on FMS energy deposits, and the anti-k_T algorithm is used within the FASTJET framework [47], with resolution parameter $R = 0.7$. The photon candidates are used as basic building units in the jet reconstruction. Similar as π^0 reconstruction, a minimum energy threshold of 0.5 GeV for 200 GeV data and 1.0 GeV for 500 GeV data is applied to the photon candidates to reduce the possible charged hadron contribution.

The reconstructed jet energy is first corrected by subtracting the contributions from the underlying event, which is estimated utilizing the so-called "off-axis cone method" [48]. For a reconstructed jet, one first defines the axes of two cones at the same pseudo-rapidity as the reconstructed jet but at angles of $\pm\pi/2$ relative to the azimuthal angle of the jet. The cone parameter used is $R = 0.7$. The energy density is calculated within each cone, where the jet area is given by the FASTJET package [47] using the ghost particle technique.

Then the jet kinematics are further corrected back to the "particle level," with a correction factor determined by a PYTHIA + GEANT simulation with same version and tune as in last subsection. We define the "particle level" as the stable particles (photons here) produced in a proton-proton event in PYTHIA prior to the GEANT simulation of detector responses. The correction factor ranges from 0.84 to 0.91 for 500 GeV data and from 0.97 to 1.03 for 200 GeV. Note that the jet reconstructed this way is a partial jet in the sense that only photons are included, and will be referred to as an electromagnetic jet (EM-jet) in order to distinguish it from a full jet. Throughout the remainder of this paper, we will refer to an EM-jet as simply a jet, unless specified otherwise.

In the jet reconstruction, no requirement on photon numbers is applied. Figure 3 shows the measured photon multiplicity distribution for reconstructed jets with jet p_T greater than 2 GeV$/c$. The average photon multiplicity is 5.6 for 200 GeV data, and 4.9 for 500 GeV data. The higher photon energy cut at 500 GeV during jet reconstruction makes the observed multiplicity smaller than that at 200 GeV.

E. Asymmetry calculation

1. π^0 and jet TSSA

Equation (3) shows the π^0 yield $N^\uparrow$ for spin "up" of the π^0 production as a function of the azimuthal angle ϕ in transversely polarized proton-proton collisions. In this equation, ϵ stands for the efficiency of the detector, $\mathcal{L}$ for the beam luminosity, and P for the beam polarization; the arrow indicates the spin direction of the beam. In order to eliminate effects due to a nonuniform detector efficiency and a time-dependent luminosity, the "cross-ratio" method is used in calculating the asymmetry, see Eq. (4).

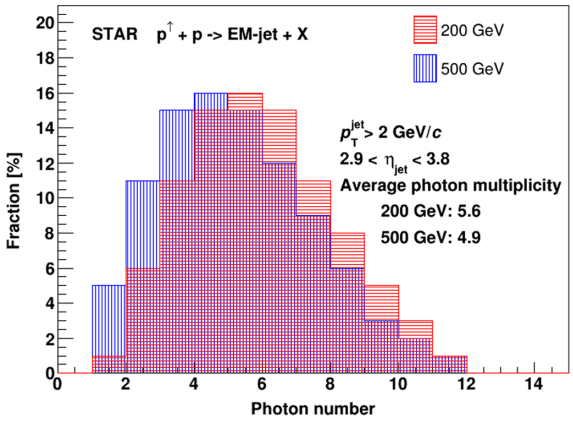

FIG. 3. The observed EM-jet multiplicity distribution with the STAR FMS detector in transversely polarized proton-proton collisions at 200 and 500 GeV.

The "cross-ratio" method [49] takes advantage of the detector symmetry, which cancels efficiency and luminosity effects to leading order. In practice, ϕ is divided into ten bins, which results in five data points on the right-hand side of Eq. (4) as a function of $\cos\phi$, which are used to extract $A_{\mathrm{N}}^{\mathrm{raw}}$:

$$\begin{aligned} N^{\uparrow}(\phi) &= \epsilon\mathcal{L}^{\uparrow}\sigma^{\uparrow}, \\ &= \epsilon\mathcal{L}^{\uparrow}(1 + P\cdot A_{\mathrm{N}}\cos\phi)\sigma_0, \end{aligned} \tag{3}$$

$$P\cdot A_{\mathrm{N}}^{\mathrm{raw}}\cos\phi = \frac{\sqrt{N^{\uparrow}(\phi)N^{\downarrow}(\phi+\pi)} - \sqrt{N^{\downarrow}(\phi)N^{\uparrow}(\phi+\pi)}}{\sqrt{N^{\uparrow}(\phi)N^{\downarrow}(\phi+\pi)} + \sqrt{N^{\downarrow}(\phi)N^{\uparrow}(\phi+\pi)}}. \tag{4}$$

The raw asymmetry $A_{\mathrm{N}}^{\mathrm{raw}}$ obtained using Eq. (4) has a contribution both from the signal and background. Assuming the background asymmetry A_{N}^{bkg} is constant over the mass region $0.0 < M_{\gamma\gamma} < 0.3$ GeV$/c^2$, the signal asymmetry $A_{\mathrm{N}}^{\pi^0}$ can be extracted by solving Eq. (5). In these equations, the uncorrected signal ($A_{\mathrm{N}}^{\mathrm{raw}_{sig}}$) and background ($A_{\mathrm{N}}^{\mathrm{raw}_{sb}}$) asymmetries are calculated in the signal region $0.0 < M_{\gamma\gamma} < 0.2$ GeV$/c^2$ for the signal and the side-band region $0.2 < M_{\gamma\gamma} < 0.3$ GeV$/c^2$ for the background. The regions are shown in Fig. 2. The signal fractions in these two regions, $f_{\mathrm{sig}_{sig}}$ and $f_{\mathrm{sig}_{sb}}$, are obtained from fits to the π^0 invariant mass distribution as shown in Fig. 2,

$$\begin{aligned} A_{\mathrm{N}}^{\mathrm{raw}_{sig}} &= f_{\mathrm{sig}_{sig}}A_{\mathrm{N}}^{\pi^0} + (1 - f_{\mathrm{sig}_{sig}})A_{\mathrm{N}}^{bkg}, \\ A_{\mathrm{N}}^{\mathrm{raw}_{sb}} &= f_{\mathrm{sig}_{sb}}A_{\mathrm{N}}^{\pi^0} + (1 - f_{sig_{sb}})A_{\mathrm{N}}^{bkg}. \end{aligned} \tag{5}$$

The extraction of the jet TSSA is almost the same as the π^0 TSSA using Eq. (4) except a slight difference on background part as detailed in Sec. III C.

2. Collins asymmetry

The extraction of Collins asymmetry (A_{UT}) is similar to that of the π^0 TSSA. Because of the different definition of the azimuthal angle, the cross-ratio method needs to be modified to account for the Collins angle $\phi_{\mathrm{C}} = \phi_{\mathrm{S}} - \phi_{\mathrm{H}}$, see Eq. (6). For the Collins angles we follow the same definition as in Ref. [34]. ϕ_S is the angle between the upward spin direction of the polarized proton and the plane spanned by the momenta of the jet and the beam. The angle ϕ_{H} is the angle between the jet-beam plane and the jet-pion plane determined by the π^0 momentum and the jet momentum.

$$P\cdot A_{\mathrm{UT}}\sin\phi_{\mathrm{C}} = \frac{\sqrt{N^{\uparrow}(\phi_{\mathrm{C}})N^{\downarrow}(\phi_{\mathrm{C}}+\pi)} - \sqrt{N^{\downarrow}(\phi_{\mathrm{C}})N^{\uparrow}(\phi_{\mathrm{C}}+\pi)}}{\sqrt{N^{\uparrow}(\phi_{\mathrm{C}})N^{\downarrow}(\phi_{\mathrm{C}}+\pi)} + \sqrt{N^{\downarrow}(\phi_{\mathrm{C}})N^{\uparrow}(\phi_{\mathrm{C}}+\pi)}}. \tag{6}$$

The π^0 reconstruction here is slightly different from the inclusive π^0 reconstruction as in Sec. II C. Since the π^0 is part of a jet, one needs to iterate over all combinations of photons within the jet. To avoid double-counting, photons can only be used once to reconstruct a π^0. In practice, the reconstruction starts with the highest energy π^0 candidate. If it passes all the selection cuts, its constituent photons will be excluded from the subsequent reconstruction. If it doesn't, the second highest energy π^0 candidate is checked, and so on, until a qualified candidate is found. The reconstruction continues with the next highest energy π^0 candidate from the remaining photons until all π^0 candidates have been evaluated. For this way of π^0 reconstruction, we do not perform a background subtraction for the Collins asymmetry. The possible influence from the background is studied through the mass dependence of the asymmetry as discussed in Sec. IV D.

III. CORRECTIONS AND SYSTEMATIC UNCERTAINTIES

A. Energy uncertainty

The photon energy uncertainty includes contributions from calibration, nonlinear detector responses, and radiation damage. The contributions of the three types of energy uncertainties are 3.5%, 1.5%, and 2.2% for 500 GeV data and 2.5%, 1.5%, and 0.5% for 200 GeV data, respectively. The overall photon energy uncertainty is 4.4% for 500 GeV data and 3.0% for 200 GeV data.

The π^0s and jets are composed of multiple photons. Their energy uncertainties are related to the energy of each of the constituent photons, and differ for every case. However, an upper limit for the energy uncertainty of a π^0/jet can be estimated using the constituent photon energy uncertainties. This estimation shows that the π^0 energy uncertainty is less than 4.4% for 500 GeV data and 3.0% for 200 GeV data. For the jet energy, additional uncertainties related with the energy correction factor to particle level are considered, which are estimated from simulation to be 6.4% for 500 GeV and 8.0% for 200 GeV data. These estimations show that the final jet energy uncertainty is less than 7.8% for 500 GeV and 8.5% for 200 GeV data. The details on these energy uncertainties can found be in Ref. [50].

In this paper, the π^0 TSSA is extracted as a function of Feynman-x and p_{T}. Feynman-x is defined as $x_{\mathrm{F}} = 2p_{\mathrm{L}}/\sqrt{s}$, and p_{L} is the longitudinal momentum. It approximately equals the π^0 energy divided by the proton beam energy. Its uncertainty is the same as the one for the π^0 energy. Since the photon angular uncertainty is much smaller than the energy uncertainty, the π^0 p_{T} uncertainty is also dominated

by the π^0 energy. In summary, the uncertainties of x_F and p_T for π^0 TSSA are 4.4% for 500 GeV and 3.0% for 200 GeV data. The jet TSSA is presented versus x_F in Sec. IV C, and the x_F uncertainties are 7.8% for 500 GeV and 8.5% for 200 GeV data.

The Collins asymmetries are measured as a function of z_{em}, which is the fraction of the π^0 energy over the jet energy, $z_{em} = E_{\pi^0}/E_{jet}$. The uncertainty of z_{em} can be estimated using the uncertainty on the ratio of π^0 energy and jet energy. This is found to be less than 8.9% for 500 GeV and 9.0% for 200 GeV data.

B. The π^0 TSSA

As discussed earlier, the two fractions $f_{\mathrm{sig}_{sig}}$ and $f_{\mathrm{sig}_{sb}}$ in Eq. (5) needed to calculate the TSSA are obtained from fits to the π^0 invariant mass distribution. The uncertainty of the fractions as obtained from the fit are propagated to the π^0 TSSA as a source of systematic uncertainty. It is found that this uncertainty is up to 5.8% of the magnitude of the asymmetry. This systematic uncertainty is smaller than the marker size in the TSSA result plots in the next section.

C. The Jet TSSA

The 200 GeV data set contains a small number of jets reconstructed with energy far above the beam energy. These nonphysical events serve as a background under the jet signal, which may come from the pile up of noncollision background to normal events. The asymmetry of these events is consistent with zero. We assume these events also exist at lower energy, which will decrease the measured jet TSSA. The asymmetries can be corrected using a background subtraction, with a correction factor $1/(1-r)$, where r is the background fraction in the specified energy range. To estimate the background fraction, we choose the jet events in the energy range of 120 GeV to 150 GeV as pure background events. The energy spectrum of these events is found to be following a linear trend. A linear fit is done in this energy range and extrapolated to lower energy to estimate the background fraction. Results using this method show the highest background fraction is about 3% for the highest x_F bin.

D. The Collins asymmetry

The resolution of the Collins angle, ϕ_C, used in the calculation of the Collins asymmetry, is limited by the resolution of the photon position and jet axis. The resolution can be obtained from Monte Carlo simulations by comparing the reconstructed ϕ_C on detector and particle levels. The smearing of this angle tends to underestimate the asymmetry and this effect can be corrected by multiplying a correction factor to the raw asymmetries. The resulting correction factor ranges from 1.01 to 1.04 in the region of $0.3 < z_{em} < 0.9$.

IV. RESULTS

The clockwise-circulating RHIC beam (blue) faces the FMS. Single-spin asymmetries measured with respect to the blue beam polarization correspond to positive x_F. The asymmetries with respect to the polarization of the counterclockwise circulating beam (yellow), which corresponds to negative x_F, are consistent with zero. This has been observed in multiple experiments [3–5]. Therefore, the results with negative x_F are not shown. Please note that there is a general scale uncertainty of 3.0/3.4% for 200/500 GeV data from beam polarization for all spin asymmetries in this section, which is not included in the plots.

A. The π^0 TSSA

Figure 4 shows the results of the π^0 TSSA for 200 GeV (red points) and 500 GeV (blue points) transversely polarized proton-proton collisions as a function of x_F. The lower panel shows the average π^0 p_T for each x_F bin. The asymmetry increases with x_F. The x_F of 200 GeV data reach up to 0.6, where the largest asymmetry is observed. The results of both data sets are consistent in the overlapping region, $0.2 < x_F < 0.35$. For both energies, the background asymmetries, which are not shown in the figure, are consistent with zero.

Figure 5 shows the TSSA result as a function of π^0 p_T, in the overlap x_F region, $0.18 < x_F < 0.36$, for the two data sets. The three panels represent different regions in x_F. Although the statistics for the 500 GeV data are limited, it

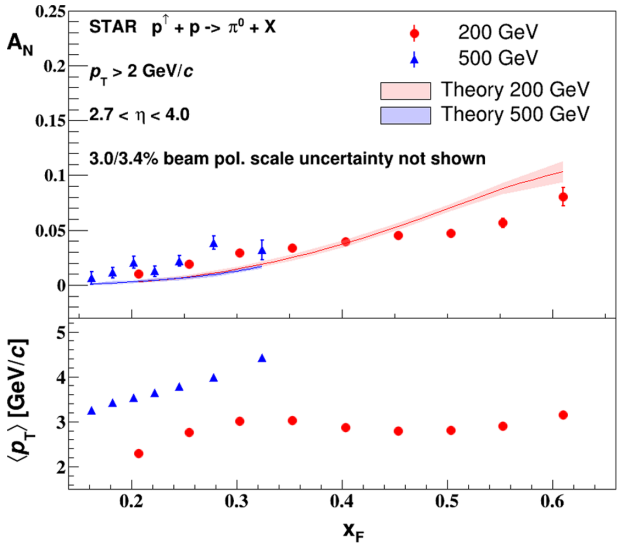

FIG. 4. Transverse single-spin asymmetry (A_N) as a function of x_F for π^0 production in transversely polarized proton-proton collisions at $\sqrt{s} = 200$ and 500 GeV. The error bars are statistical uncertainties only. A systematic uncertainty up to 5.8% of A_N for each point is smaller than the size of the markers. The average p_T of the π^0 for each x_F bin is shown in the lower panel. Theory curves based on a recent global fit [51] are also shown.

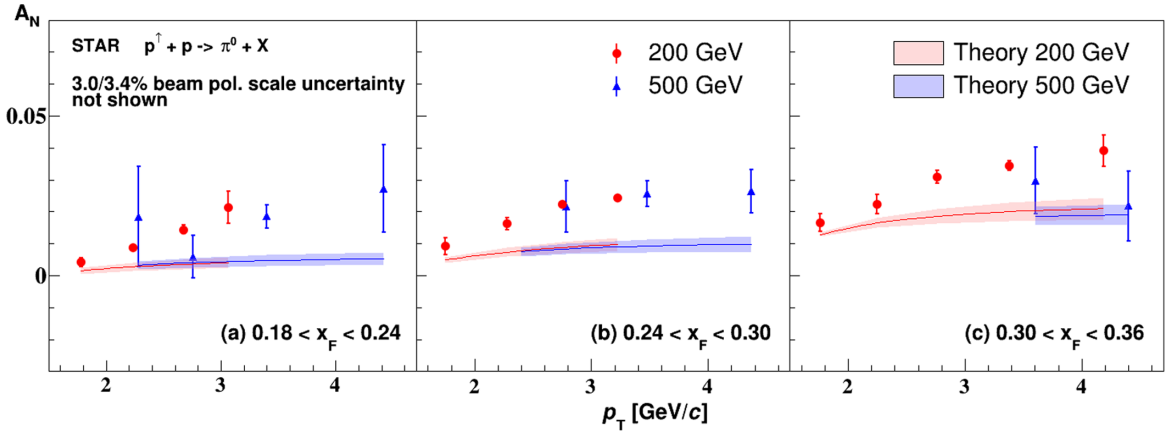

FIG. 5. The transverse single-spin asymmetry as a function of the π^0 p_T for three different x_F ranges, (a), (b), and (c), for transversely polarized proton-proton collisions at $\sqrt{s} = 200$ and 500 GeV. The error bars are statistical uncertainties only. A systematic uncertainty up to 5.8% of A_N for each point is smaller than the size of the markers. Theory curves based on the recent global fit [51] are also shown.

can be seen that the results at the two beam energies are consistent. In the x_F regions covered by the data, the 200 GeV results show the asymmetries rise with p_T, clearly indicating a dependence of the asymmetry on p_T and x_F. This is consistent with similar observations in previous STAR measurements [3]. More details regarding the p_T dependence at 200 GeV can be found in Ref. [35].

Figure 6 shows the comparison of these STAR results with the other existing measurements in transversely polarized proton-proton collisions. They include previous STAR measurements using the FPD detector [3], results from the RHICf experiment [5], the PHENIX experiment [4], and the E704 experiment [2] at the Fermi National Accelerator Laboratory. The average p_T of the π^0 for each x_F bin is shown in the lower panel. The π^0 TSSA results in this paper are consistent with the other measurements. This can only be explained with a very weak scale dependence of the π^0 TSSA for a $\sqrt{s}$ range of 19.4 to 510 GeV. The earlier 200 GeV STAR results [3] seem to be slightly lower than the current 2015 results in the range of $x_F < 0.4$. This could be explained by the p_T dependence of the TSSA results. From the above discussion, the TSSA results are not only a function of x_F, but also a function of the p_T. At the same x_F range, the asymmetries rise with the p_T in the region $1\ \text{GeV}/c < p_T < 3\ \text{GeV}/c$. The lower panel of Fig. 6 shows that the mean p_T as a function of x_F in the region of $x_F < 0.4$ in this paper are higher than those of the earlier 200 GeV STAR results.

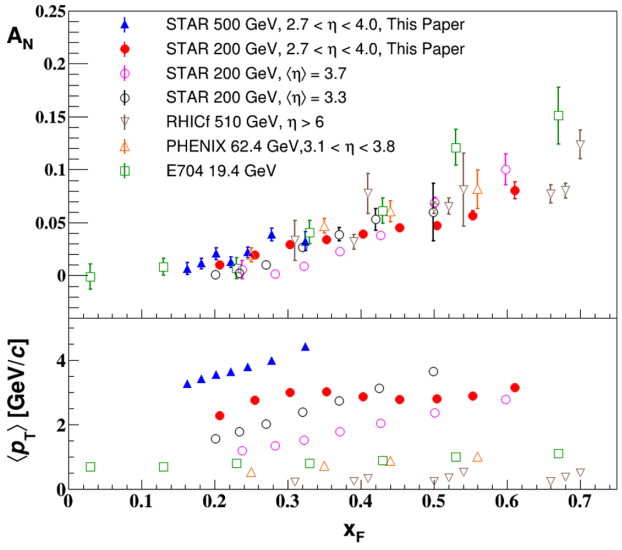

FIG. 6. Comparison of this measurement of the transverse single-spin asymmetry as a function of x_F for inclusive π^0 with previous measurements from $\sqrt{s} = 19.4$ GeV to $\sqrt{s} = 510$ GeV in transversely polarized proton-proton collisions. The error bars are statistical uncertainties only. The average p_T of the π^0 for each x_F bin is shown in the lower panel.

B. The TSSA for isolated π^0

In searching for the origin of the transverse single-spin asymmetry, one particularly interesting aspect is the topological dependence of π^0 TSSAs, meaning one divides the π^0 sample into subgroups based on the event structure. One group contains the isolated π^0s, which refers to the π^0s with no other surrounding photons. The other group contains the nonisolated π^0s, which are accompanied by other photons. In practice, the energy fraction z_{em}, which is the π^0 energy over the jet energy, is used to determine whether or not a π^0 is isolated. Two photons alone can be reconstructed as a jet, so a π^0 would be identified as isolated when its z_{em} is close to 1. In the following step, one applies $z_{em} > 0.98$ to select isolated π^0 and $z_{em} < 0.9$ for the nonisolated ones. The gap ensures a clean separation between the two groups.

In this way, both types of π^0s always correlate with a jet. Therefore, its constituent photons should be limited within the same jet. The π^0 selection and asymmetry calculation remain the same. The jet resolution parameter $R = 0.7$ indicates the area where the π^0 is considered to be isolated.

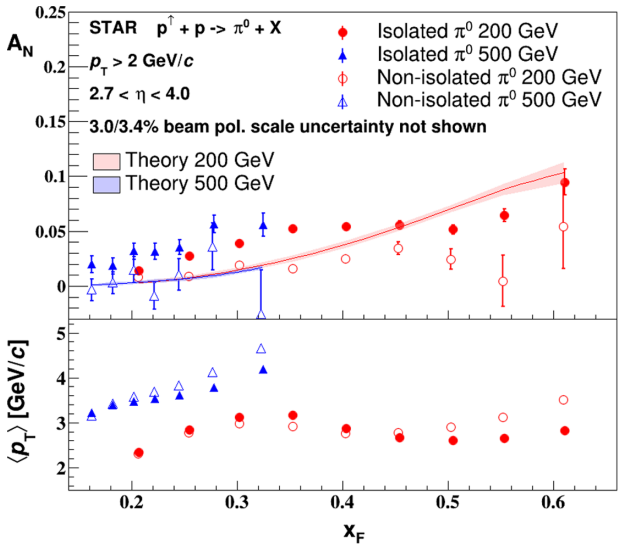

FIG. 7. The transverse single-spin asymmetry as a function of x_F for the isolated and nonisolated π^0 in transversely polarized proton-proton collisions at $\sqrt{s} = 200$ and 500 GeV. The error bars are statistical uncertainties only. A systematic uncertainty up to 5.8% of A_N for each point is smaller than the size of the markers. Theory curves based on a recent global fit [51] are also shown. The average p_T of the π^0 for each x_F bin is shown in the lower panel.

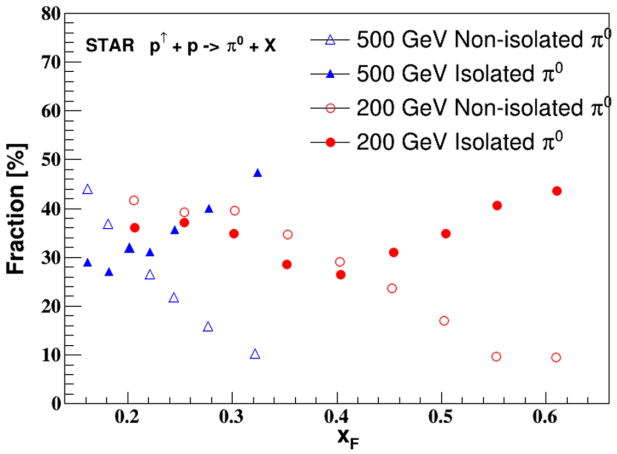

FIG. 8. Fractions of isolated and nonisolated π^0 to the overall inclusive π^0 sample in the mass region 0–0.3 GeV/c^2, after background subtraction. The missing fraction mainly includes the events between the isolated cuts: $0.9 < z_{em} < 0.98$.

Figure 7 shows the TSSA of these two types of π^0. Although the asymmetries of both types increase with x_F, their magnitudes are significantly different. The asymmetries for the isolated π^0 are clearly larger than the asymmetries for the nonisolated π^0. This result suggests there could be different mechanisms in play to explain the large asymmetries shown in Fig. 4. The nonisolated π^0s are considered to be part of a jet, which has fragmented from a parton, while the underlying subprocess for the isolated ones is not yet clear. One possible explanation is that a significant part of the isolated π^0s are from diffractive processes [52], which needs further confirmation. The theoretical descriptions mentioned in the introduction would mainly apply to the TSSA of the nonisolated π^0s, which usually assume all the π^0s come from parton fragmentation, for example in a recent global analysis [51]. A recent measurement of TSSA for very forward π^0 in transversely polarized proton-proton collisions by the RHICf experiment also indicates that the diffractive process could give a sizable asymmetry [5].

To understand the contributions from isolated and nonisolated π^0 to the overall π^0 TSSA, Fig. 8 shows the fractions of each type in the overall π^0 sample. It is noted that these fractions are background corrected to ensure the fractions represent the π^0 signal only. It can be seen that, for each data set, the isolated π^0 plays an important role in the high x_F region where the asymmetry is significantly larger. In Ref. [35], a somewhat different isolation criterion was used, but the same conclusion was obtained that the isolated π^0 have larger TSSA than the nonisolated π^0 in $p + \mathrm{Al}$ and $p + \mathrm{Au}$ collisions in addition to proton-proton collisions.

C. The Jet TSSA

Figure 9 shows the results of the jet TSSA as a function of x_F for both data sets. The solid symbols in the figure represent the results that have no limitation on the photon multiplicity when reconstructing the jet, while the open symbols represent the results that required the observed photon multiplicity in the jet to be greater than 2. The asymmetries are nonzero and increase with x_F, similar to the π^0 TSSA. The consistency of the 200 and 500 GeV jet asymmetries in the overlap region suggests a weak energy dependence. However, the jet asymmetries are much smaller than the π^0 ones in Fig. 4 for the same x_F. Theoretically, the jet asymmetry is believed to be dominated by initial-state effects related with the Sivers function.

Since a single photon or two photons can be reconstructed as a jet, the isolated π^0 sample described earlier is part of the jet sample and therefore enhances the overall jet TSSA. The open symbols in Fig. 9 show the TSSA for jets with a measured photon multiplicity greater than 2. The jet TSSAs with a minimum multiplicity requirement are smaller than the ones without this requirement, while the p_T at each x_F of the two samples is almost the same. The 200 GeV results are significantly larger than zero, while the 500 GeV results are consistent with zero within uncertainties, which may indicate a stronger energy dependence than what was observed for the π^0 TSSA.

The black crosses in Fig. 9 represent the results from the $A_N DY$ Collaboration at RHIC [28] with transversely polarized proton-proton collisions at 500 GeV. The $A_N DY$

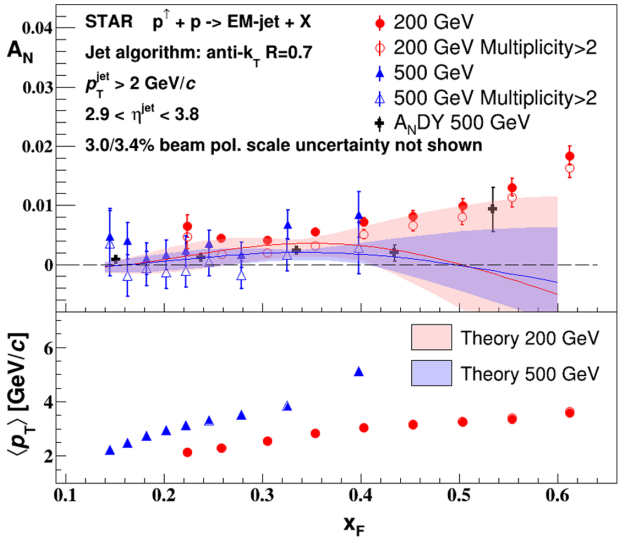

FIG. 9. Transverse single-spin asymmetry as a function of x_F for electromagnetic jets in transversely polarized proton-proton collisions at $\sqrt{s} = 200$ and 500 GeV. The error bars are statistical uncertainties only and the systematic uncertainties are negligible. The results that require more than two photons observed inside a jet are shown as open symbols. The previous measurements for full jets at 500 GeV reported by the $A_N DY$ Collaboration [28] are also plotted. Theory curves [30] for TSSA of full jets at mean rapidity $\langle y \rangle = 3.25$ for 200 GeV (red) and $\langle y \rangle = 3.57$ for 500 GeV (blue) are also shown. The average p_T of the jet for each x_F bin is shown in the lower panel.

experiment measured jets using an electromagnetic and a hadronic calorimeter to reconstruct both the electromagnetic and hadronic components of jets. The $A_N DY$ result suggests the jet TSSA are very small and they are close to the STAR jet TSSA result measured at 500 GeV with the minimum multiplicity requirement. The consistency of these two results suggests that the TSSA for EM-jets probes the same underlying physics as full jets.

D. The Collins asymmetry

The Collins effect is defined as a nonuniform azimuthal distribution of a particle's p_T in the hadronization of a transversely polarized quark [12]. By measuring the Collins asymmetry of π^0 within a jet, one can directly study the fragmentation process contribution to the single-spin asymmetry at forward rapidities. The Collins angle (ϕ_C) in Eq. (6) is defined in the same way as in Ref. [34]. The resolution of the Collins angle is the major source of the asymmetry uncertainty. If the direction of the π^0 momentum is close to the jet thrust axis, for example at high z_{em}, the uncertainty of the ϕ_C angle becomes large. Therefore, a ΔR cut, $\Delta R = \sqrt{((\eta_{\pi^0} - \eta_{\rm jet})^2 + (\phi_{\pi^0} - \phi_{\rm jet})^2}$, has been applied in the analysis to reject such events. The value of this cut was balanced between the benefit of excluding those events with large uncertainty and the loss of statistics at high z_{em}. We determined $\Delta R > 0.04$ to be the best choice, which is the same as in Ref. [34].

As mentioned in Sec. II E 2, there is no background subtraction for the Collins asymmetry. Nevertheless, the influence of possible background can be studied through the mass dependence of the asymmetry. The π^0 signal is concentrated in the mass region $M_{\gamma\gamma} < 0.2$ GeV/c^2, whereas the background fraction changes significantly as a function of mass from the region $M_{\gamma\gamma} < 0.2$ GeV/c^2 to the region $M_{\gamma\gamma} > 0.2$ GeV/c^2. A comparison of the Collins results in the region of (0, 0.2 GeV/c^2) and those in the region of (0.2, 0.3 GeV/c^2) did not show a clear mass dependence in both data sets.

The jet p_T is required to be larger than 2 GeV/c. The average jet p_T is 3.8 GeV/c for 500 GeV data and 3.0 GeV/c for 200 GeV data. The average jet pseudorapidity is 3.1 for 500 GeV data and 3.3 for 200 GeV data. Figure 10 shows the measured Collins asymmetries (A_{UT}) originating from the final-state effect, for both the 200 and 500 GeV data. Both results show very small asymmetries within uncertainties.

The π^0 momentum transverse to the jet axis, j_T, can be used to measure how close the π^0 is to the jet axis. An investigation of the dependence of the Collins asymmetry on j_T at 200 GeV is presented in Fig. 11. The Collins asymmetries are separated into four j_T bins. It is found that the asymmetries for $j_T > 0.2$ GeV/c show a tendency to be negative. This j_T dependence can be used to further constrain TMD models.

E. Comparison to models

We compare our results to the theoretical calculations that can be seen in Figs. 4, 5, 7, 9, and 10. The calculations

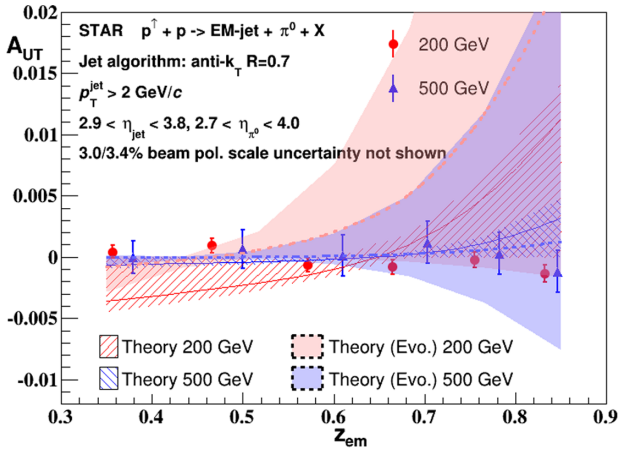

FIG. 10. The Collins asymmetry for π^0 in an electromagnetic jet for transversely polarized proton-proton collisions at $\sqrt{s} = 200$ and 500 GeV. The error bars are statistical uncertainties only and the systematic uncertainties are negligible. Theory curves for the Collins asymmetry of a π^0 in a full jet with or without TMD evolution [31] are also shown.

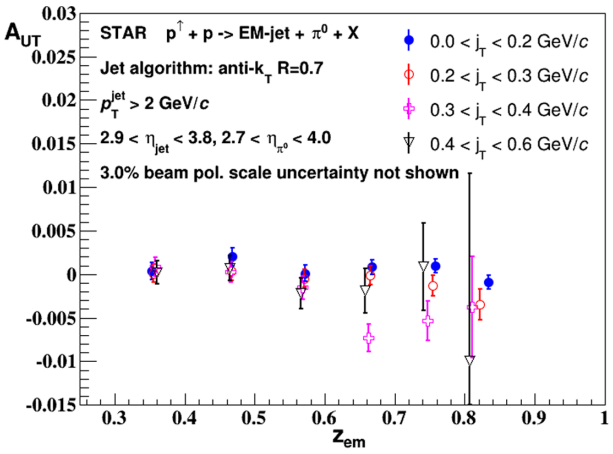

FIG. 11. The j_T dependence of the π^0 Collins asymmetry in transversely polarized proton-proton collisions at $\sqrt{s} = 200$ GeV. The error bars are statistical uncertainties only and the systematic uncertainties are negligible.

of π^0 TSSA [51], jet TSSA [30] and Collins asymmetry [31] are based on the TMD and collinear Twist-3 functions that have been extracted from semi-inclusive deep inelastic scattering, Drell-Yan, e^+e^- annihilation into hadron pairs, and transversely polarized proton-proton collisions that included also previous forward π^0 and charged hadron TSSA data from RHIC. The calculations refer to the kinematics of the data in this paper to account for the known kinematic dependencies of the measurements.

As shown in Figs. 4 and 5, the calculations have almost no energy dependence [51]. They underestimate the π^0 TSSA in the lower x_F region for both 200 and 500 GeV data, but overestimate it in the higher x_F region where 200 GeV data are available. In Fig. 5, the calculations show the same trend of asymmetries rising with p_T as the data, but the magnitude of the predicted asymmetry is much smaller than the measurements.

The theory curves in Fig. 7 are identical to the ones in Fig. 4. In the x_F region lower than 0.3, they can describe the nonisolated π^0 TSSA measurements, in which these π^0s are considered to originate from fragmentation. The theory curve in this region is mostly constrained by the Sivers/Collins inputs from SIDIS data [51].

For the jet TSSA in Fig. 9, the calculation for 500 GeV is consistent with the measurement that has the minimum photon multiplicity requirement and also the full jet result from the $A_N DY$ experiment. However, the calculation for 200 GeV predicts the asymmetry to fall with x_F, which contradicts our measurement. It is noted that the theoretical uncertainty bands are substantial [30].

For the Collins asymmetry in Fig. 10, two sets of theory curves represent the cases with or without the TMD evolution being taken into account [31]. Our j_T combined results for both collision energies are consistent with zero, which are within the uncertainty bands of the two calculations.

V. CONCLUSION

We report the measurements of transverse single-spin asymmetries for π^0s in the forward rapidity region in transversely polarized proton-proton collisions at 200 GeV and 500 GeV using the FMS detector at STAR. The measurement at 200 GeV was done with the largest data sample thus far. The asymmetries increase with x_F. No energy dependence was found when comparing the current results with previous data at RHIC and FNAL with center-of mass energies as low as 19.4 GeV. The transverse single-spin asymmetries for isolated and nonisolated π^0 at both 200 GeV and 500 GeV were also presented. The asymmetries of isolated π^0s are significantly larger than those of nonisolated π^0s.

The transverse single-spin asymmetries for electromagnetic jets were measured with the FMS in transversely polarized proton-proton collisions at both 200 GeV and 500 GeV. The 500 GeV result with a minimum photon multiplicity requirement is consistent with zero, which coincides with the full jet measurement from the $A_N DY$ experiment. The 200 GeV results are small, but are clearly nonzero within uncertainties.

Collins asymmetries for π^0s within an electromagnetic jet were measured in transversely polarized proton-proton collisions at both 200 GeV and 500 GeV. The asymmetries are small across the z_{em} bins and might exhibit a j_T dependence at 200 GeV. The latter could help to constrain TMD models and needs theoretical predictions.

These new data provide important information for understanding the underlying physics mechanism for the transverse single-spin asymmetry. In particular, the observed small TSSA for nonisolated π^0s and also small Collins asymmetries with EM-jets suggest that the Collins effect itself cannot account for the observed π^0 TSSA. On the other hand, the observed small TSSA for electromagnetic jets indicates the contribution from the Sivers effect cannot be the dominant source of π^0 TSSA, either. The sizable TSSA for isolated π^0 thus indicates a new mechanism, likely diffractive process, could be a significant source for the π^0 TSSA in transversely polarized proton-proton collisions at RHIC, and more theory efforts and dedicated measurements are called for to have a complete understanding on this aspect.

ACKNOWLEDGMENTS

We thank the RHIC Operations Group and RCF at BNL, the NERSC Center at LBNL, and the Open Science Grid consortium for providing resources and support. This work was supported in part by the Office of Nuclear Physics within the U.S. DOE Office of Science, the U.S. National Science Foundation, the Ministry of Education and Science of the Russian Federation, the National Natural Science Foundation of China, the Chinese Academy of Science, the Ministry of Science and Technology of China, the Chinese Ministry of Education, the Higher Education Sprout Project

by Ministry of Education at NCKU, the National Research Foundation of Korea, the Czech Science Foundation and Ministry of Education, Youth and Sports of the Czech Republic, Hungarian National Research, Development and Innovation Office, the New National Excellency Programme of the Hungarian Ministry of Human Capacities, the Department of Atomic Energy and Department of Science and Technology of the Government of India, the National Science Centre of Poland, the Ministry of Science, Education and Sports of the Republic of Croatia, RosAtom of Russia and German Bundesministerium fur Bildung, Wissenschaft, Forschung and Technologie (BMBF), Helmholtz Association, Ministry of Education, Culture, Sports, Science, and Technology (MEXT) and the Japan Society for the Promotion of Science (JSPS).

[1] R. Klem, J. Bowers, H. Courant, H. Kagan, M. Marshak, E. Peterson, K. Ruddick, W. Dragoset, and J. Roberts, Phys. Rev. Lett. **36**, 929 (1976).
[2] D. Adams *et al.* (E581/E704 Collaboration), Phys. Lett. B **261**, 201 (1991).
[3] B. Abelev *et al.* (STAR Collaboration), Phys. Rev. Lett. **101**, 222001 (2008).
[4] A. Adare *et al.* (PHENIX Collaboration), Phys. Rev. D **90**, 012006 (2014).
[5] M. Kim *et al.* (RHICf Collaboration), Phys. Rev. Lett. **124**, 252501 (2020).
[6] G. L. Kane, J. Pumplin, and W. Repko, Phys. Rev. Lett. **41**, 1689 (1978).
[7] Z.-T. Liang and C. Boros, Int. J. Mod. Phys. A **15**, 927 (2000).
[8] U. D'Alesio and F. Murgia, Prog. Part Nucl. Phys. **61**, 394 (2008).
[9] K.-B. Chen, S.-Y. Wei, and Z.-T. Liang, Front. Phys. **10**, 101204 (2015).
[10] X. Ji, J.-W. Qiu, W. Vogelsang, and F. Yuan, Phys. Rev. Lett. **97**, 082002 (2006).
[11] D. W. Sivers, Phys. Rev. D **41**, 83 (1990).
[12] J. C. Collins, Nucl. Phys. **B396**, 161 (1993).
[13] J. C. Collins, S. F. Heppelmann, and G. A. Ladinsky, Nucl. Phys. **B420**, 565 (1994).
[14] A. Efremov and O. Teryaev, Sov. J. Nucl. Phys. **36**, 140 (1982).
[15] J.-W. Qiu and G. F. Sterman, Phys. Rev. Lett. **67**, 2264 (1991).
[16] D. Boer, P. Mulders, and F. Pijlman, Nucl. Phys. **B667**, 201 (2003).
[17] F. Yuan and J. Zhou, Phys. Rev. Lett. **103**, 052001 (2009).
[18] C. Boros, Z. Liang, and T. Meng, Phys. Rev. Lett. **70**, 1751 (1993).
[19] C. Kouvaris, J.-W. Qiu, W. Vogelsang, and F. Yuan, Phys. Rev. D **74**, 114013 (2006).
[20] Y. Koike and K. Tanaka, Phys. Rev. D **76**, 011502(R) (2007).
[21] Z.-B. Kang and A. Prokudin, Phys. Rev. D **85**, 074008 (2012).
[22] Z.-B. Kang, F. Yuan, and J. Zhou, Phys. Lett. B **691**, 243 (2010).
[23] A. Metz and D. Pitonyak, Phys. Lett. B **723**, 365 (2013).
[24] K. Kanazawa and Y. Koike, Phys. Rev. D **88**, 074022 (2013).
[25] L. Gamberg, Z.-B. Kang, D. Pitonyak, and A. Prokudin, Phys. Lett. B **770**, 242 (2017).
[26] J. Zhou, Phys. Rev. D **96**, 034027 (2017).
[27] K. Kanazawa, Y. Koike, A. Metz, and D. Pitonyak, Phys. Rev. D **89**, 111501(R) (2014).
[28] L. Bland *et al.* (AnDY Collaboration), Phys. Lett. B **750**, 660 (2015).
[29] M. Anselmino, M. Boglione, U. D'Alesio, S. Melis, F. Murgia, and A. Prokudin, Phys. Rev. D **88**, 054023 (2013).
[30] L. Gamberg, Z.-B. Kang, and A. Prokudin, Phys. Rev. Lett. **110**, 232301 (2013).
[31] Z.-B. Kang, A. Prokudin, F. Ringer, and F. Yuan, Phys. Lett. B **774**, 635 (2017).
[32] F. Yuan, Phys. Rev. Lett. **100**, 032003 (2008).
[33] U. D'Alesio, F. Murgia, and C. Pisano, Phys. Lett. B **773**, 300 (2017).
[34] L. Adamczyk *et al.* (STAR Collaboration), Phys. Rev. D **103**, 072005 (2018).
[35] J. Adam *et al.* (STAR Collaboration), Phys. Rev. D **97**, 032004 (2018)..
[36] K. Ackermann *et al.* (STAR Collaboration), Nucl. Instrum. Methods Phys. Res., Sect. A **499**, 624 (2003).
[37] W. B. Schmidke *et al.*, RHIC polarization for runs 9-17, Brookhaven National Laboratory, Technical Report No. BNL-209057-2018-TECH (2018).
[38] C. J. Dilks, Ph.D. thesis, Penn State University, 2018.
[39] J. Adam *et al.* (STAR Collaboration), Phys. Rev. D **98**, 032013 (2018).
[40] E. Braidot, Ph.D. thesis, Utrecht University, 2011.
[41] J. Kiryluk (STAR Collaboration), in *Spin physics. Polarized Electron Sources and Polarimeters. Proceedings* (World Scientific Publishing Company, Trieste, Italy, 2005), pp. 718–721.
[42] H. Qiu (STAR Collaboration), Nucl. Phys. **A931**, 1141 (2014).
[43] W. Llope *et al.*, Nucl. Instrum. Methods Phys. Res., Sect. A **522**, 252 (2004).
[44] R. Brun, F. Bruyant, M. Maire, A. C. McPherson, and P. Zanarini, *GEANT 3: User's Guide Geant 3.10, Geant 3.11; Rev. Version* (CERN, Geneva, 1987).
[45] T. Sjostrand, S. Mrenna, and P. Z. Skands, J. High Energy Phys. 05 (2006) 026.

[46] R. Field and R. Group (CDF Collaboration), arXiv:hep-ph/0510198.
[47] M. Cacciari, G. P. Salam, and G. Soyez, Eur. Phys. J. C **72**, 1896 (2012).
[48] B. B. Abelev *et al.* (ALICE Collaboration), Phys. Rev. D **91**, 112012 (2015).
[49] G. Ohlsen and P. Keaton, Nucl. Instrum. Methods **109**, 41 (1973).
[50] Z. Zhu, Ph.D. thesis, Shandong University, 2020.
[51] J. Cammarota, L. Gamberg, Z.-B. Kang, J. A. Miller, D. Pitonyak, A. Prokudin, T. C. Rogers, and N. Sato (Jefferson Lab Angular Momentum Collaboration), Phys. Rev. D **102**, 054002 (2020).
[52] E.-C. Aschenauer *et al.*, arXiv:1501.01220.